Spatiotemporal characterization of interfacial Faraday waves by means of a light absorption technique

A. V. Kityk
Institute for Computer Science, Technical University of Czestochowa, Electrical Engineering Department, Al. Armii Krajowej 17, PL-42200 Czestochowa, Poland

J. Embs and V. V. Mekhonoshin
Theoretische Physik, Universität des Saarlandes, 66041 Saarbrücken, Germany

C. Wagner*
Experimentalphysik, Universität des Saarlandes, 66041 Saarbrücken, Germany
(Received 10 March 2005; revised manuscript received 6 July 2005; published 13 September 2005)

We present measurements of the complete spatiotemporal Fourier spectrum of Faraday waves. The Faraday waves are generated at the interface of two immiscible index matched liquids of different density. By use of a light absorption technique we are able to determine the bifurcation scenario from the flat surface to the patterned state for each complex spatial and temporal Fourier component separately. The surface spectra at onset are found to be in good agreement with the predictions from the linear stability analysis. For the nonlinear state our measurements show in a direct manner how energy is transferred from lower to higher harmonics and we quantify the nonlinear coupling coefficients. Furthermore we find that the nonlinear coupling generates static components in the temporal Fourier spectrum leading thus to a contribution of a nonoscillating permanent sinusoidal deformed surface state. A comparison of hexagonal and rectangular patterns reveals that spatial resonance can give rise to a spectrum that violates the temporal resonance conditions given by the weakly nonlinear theory.

DOI: 10.1103/PhysRevE.72.036209 PACS number(s): 89.75.Kd, 47.54.+r, 47.35.+i, 47.20.Gv

I. INTRODUCTION

The Faraday experiment is probably the first nonequilibrium pattern forming system that was investigated scientifically, namely by Michael Faraday in 1831 [1]. Nevertheless it took until only recently to become possible to determine the complete Fourier spectrum of the deformed surface state [2]. While an experimental analysis of the full mode spectrum in other pattern forming model systems like Rayleigh-Benard or Taylor Couette has been standard technique for a long time, the refraction of light at the free surface of a liquid makes the analysis of surface waves rather difficult. Quantitative information about the patterned state is important not only to verify the validity of theoretical calculations [3–5] but also to gain insight on the resonance mechanisms that *form* the patterns. The Faraday experiment is especially known for its richness of different patterns that are observed [6–11]. By using complex liquids [12], very low fill heights [13] or by introducing additional frequencies to the driving signal, complex ordered states like superlattices [2,14,15] have been recently observed. But we will demonstrate that even simple patterns like lines, squares, or hexagons observed in a single driving frequency experiment can still unveil unknown surprising characteristics.

A discussion of the earlier different attempts to reveal quantitative information on the surface elevation profile $h(r,t)$ of Faraday surface waves is given in [16]. The main difficulties follow from the difference in refractive indices of the liquid and air. The interface diffuses almost no light leading to a reflection or refraction of incident light only. To our knowledge there is only one optical method that overcomes this problem with the use of polystyrene colloids to provide light scatterers within the fluid [17], but the method was only used in a turbulent regime. Another powerful method for the investigation of capillary waves on ferrofluids based on x-ray absorption was presented in [18], but the related costs and efforts might be justified for fully opaque liquids only. A remarkable study of local surface deformation measurements by use of a focused laser beam is given by Westra *et al.* [19]. These authors also present quantitative data regarding the temporal phases and find good agreement with theoretical calculations, but the local character of the measurements prevents a determination of discrete spatial Fourier modes. Another study of local surface heights based on laser induced fluorescence was presented by Lommer and Levinsen [20]. Finally a spatial extended light deflection method combined with local temporal measurements was presented by Arbell and Fineberg [21].

To bypass the problems associated with light refraction and reflection on a liquid-air interface we chose to study the interface between two index matched liquids. The upper fluid is transparent, the lower one is dyed. In the presence of surface deformations the spatial distribution of the instantaneous thickness can be deduced from the intensity of the light passed through this layer. From a hydrodynamic point of view the replacement of the air by a second liquid is nothing but a change of viscosity and density. The low kine-

*Electronic address: c.wagner@mx.uni-saarland.de

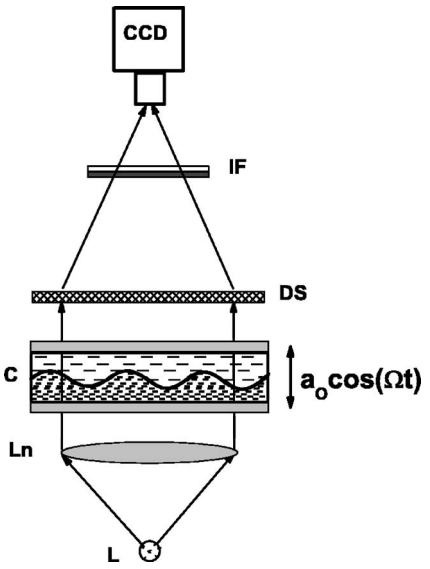

FIG. 1. Experimental setup: L—halogen lamp, Ln—lens, C—container filled by two liquids: SOIL and WSS with the same refractive indices, DS—diffusive screen, IF—interference filter, CCD—high speed CCD camera.

matic viscosity of air simplifies the theoretical calculations only. However, already the first exact theoretical analysis of the linear stability problem by Kumar and Tuckerman [3] has been made for a more general case, i.e., for a system consisting of two liquid layers and recently experimental studies on two liquid systems came more into focus [22].

II. EXPERIMENTAL SETUP

The experimental setup is shown in Fig. 1. The container consists of an aluminium ring (diameter $D=18$ cm) separating two parallel glass windows by a gap of 10 mm. It is filled by two nonmiscible liquids: a silicone oil [SOIL, Dow Corning, (Midland, Michigan) viscosity $\eta=20$ mPas, density $\rho=949$ kg/m^3) and an aqueous solution of sugar and $NiSO_4$ (WSS, $\eta=7.2$ mPas $\rho=1346$ kg/m^3). The liquid-liquid interfacial tension has been determined with the pending droplet method to $\sigma=35\pm2$ dynes/cm yielding a capillary length of $\ell_c=\sigma/(\Delta\rho g)^{1/2}=3$ mm, with g the Earth acceleration, $\Delta\rho$ the differences in the fluid densities. Our measurements were performed at a wavelength range of 5 to 15 mm, thus we observed capillary-gravity waves. The ratio of the filling heights SOIL/WSS was 8.4/1.6. The choice of the low fill height for the lower liquid was made in order to obtain a variety of different patterns, including a transition from squares to hexagons [23]. Nevertheless a theoretical analysis of critical accelerations yields that our experiments are in the infinite depth limit except for the $\Omega=12$ Hz measurement where the amount of bulk and bottom damping is approximately equal and the richest pattern dynamics occur. The sugar concentration has been adjusted to match the refractive index to the covering silicone oil layer ($n\simeq1.405$) with a precision of 5×10^{-4}. The Ni^{2+} ions produce a broad absorption band in the spectral region 600–800 nm and provide high contrast patterns projected on the diffusive screen. The container is illuminated from below with parallel light, and a bandpass optical filter in front of the camera was used to detect only wavelengths $\lambda=(655\pm5)$ nm. By varying the intensity of the lamp the flat interface has been set on a level of about 50% of the maximum optical transmission. At a $NiSO_4$ concentration of 25 wt % the contrast between the light intensity passing through crests and valleys of the wave pattern was optimum. The associated coefficient of optical absorption was measured with UV-vis spectrometry as $\alpha=6.6\pm0.1$ cm^{-1}. The absorption coefficient α does not depend on the light intensity, at least in the range of our experiments. In order to avoid uncontrolled changes of the viscosity, density, and interfacial tension of both liquids all the measurements have been performed at a constant temperature (23 ± 0.1 °C). The Faraday waves were excited by an electromagnetic shaker vibrating vertically with an acceleration in the form $[a(t)=a_0\cos(\Omega t)]$. The driving signal came from a computer via a digital/analog (D/A) converter and the acceleration was measured by a piezoelectric sensor. A self-developed closed loop algorithm was used to suppress higher harmonics $n(\Omega t)$ in the driving signal to guarantee monochromatic driving. Faraday patterns were recorded in the following way: A high speed (500 Hz, 256×256 pixels) 8-bit charge-coupled device (CCD) camera was mounted above the diffusive screen. Pictures were taken synchronously to the external driving. For a certain instant t_o the surface elevation of the Faraday patterns $h(x,y,t_o)$ is given by

$$h(x,y,t_o)=\frac{1}{\alpha}\ln\frac{I_r(x,y)}{I_p(x,y,t_o)}, \tag{1}$$

where $I_r(x,y)$ and $I_p(x,y,t_o)$ are two-dimensional (2D) intensity distributions captured by the camera for the reference picture (flat interface, $a_o=0$) and for the Faraday pattern ($a_o\neq0$), respectively. Consequently, the surface elevation function $h(x,y,t)$ is Fourier transformed and the time evolution of the Fourier amplitudes and phases of spatial modes is extracted. The use of a high speed camera compared to the earlier measurements by some of the coauthors ([2]) allows for a better temporal resolution and the method is not sensitive to distortions (defects) on time scales of several periods. The logarithm of the intensity profile renders the dynamic range nonlinear, and with an 8-bit dynamical range the resolution is approximately 1% (2%) at small (high) surface elevations, relative to the maximal surface heights. An analysis based on geometrical optics shows that errors that might result from the remaining differences in the indices of refraction are below the experimental resolution. The validity of the method has been also checked with flat layers of colored liquids of different thicknesses and the same accuracy was found. However, one should note that the Fourier transformation integrates over many pixels thus a significantly better resolution is expected.

III. LINEAR REGIME AND BEYOND

The experiments were performed by quasistatically ramping the driving amplitude for the frequencies $f=\Omega/2\pi=12$, 16, 20, 29, and 57 Hz from slightly below the critical accel-

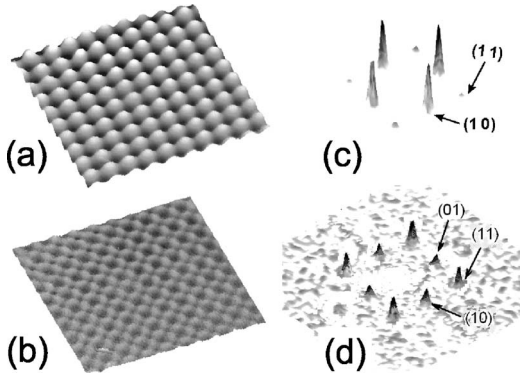

FIG. 2. Snapshots of the square Faraday pattern [(a) and (b)] and their power spectra [(c) and (d)] at $\Omega/2\pi=12$ Hz and $\varepsilon=0.17$ ($a_0=30.0$ m/s^2) for two different temporal phases corresponding to maximum [(a)] and minimum [(b)] surface elevation as indicated by arrows (t_1 and t_2) in Fig. 4.

eration a_c [$\varepsilon=(a-a_c)/a_c=-0.02$] up to just below the acceleration where the interface disintegrates and droplets occur. In the same form a ramp was driven down to check for hysteretic effects, of which none were found. For each amplitude step a series of pictures were taken and then Fourier transformed. Typically the pattern occurs in the center region of the container first but evolves in a range of $\Delta\varepsilon=0.02$. From the Fourier transformation of the pictures captured at $-0.02<\varepsilon<0.1$ (Fig. 2) the critical acceleration a_c and the critical wave-number k_c has been determined (Fig. 3).

They can be compared with the results from the theoretical linear stability analysis that has been performed by using the algorithm proposed by Kumar and Tuckerman [3]. The agreement between theory and experiment is very good, similar to former studies at the liquid air interface [24,25]. However, with our method we might be able to verify more predictions from the linear theory. Linear theory only treats transient amplitudes that are growing exponentially in time while all experiments mentioned below have been performed when the amplitudes were fully saturated. Their size and their symmetry are determined by the *nonlinearities* of the problem but one could speculate that near onset the influence

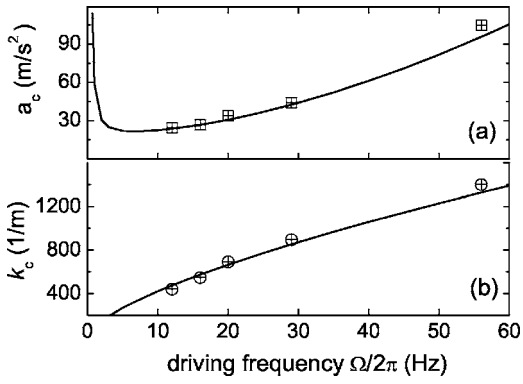

FIG. 3. Critical acceleration a_c [(a)] and critical wave number k_c [(b)] for different driving frequencies Ω. The symbols are the experimental data, the lines are theoretical calculations based on the linear stability analysis. The size of the symbols coincides with the size of the error bars.

of the nonlinearities on the relative distribution of temporal components in the spectrum of the basic modes is weak, especially if the data are extrapolated to $\varepsilon=0$.

It is a particular feature of the Faraday experiment, that at onset only one wave-number k_c becomes unstable, but the temporal spectrum already contains multiples of the fundamental oscillation frequency ω at onset. We are in the regime of subharmonic response and the fundamental oscillation frequency at onset is always $\omega=\Omega/2$ but the spectrum contains also $(n+1/2)\Omega$ frequency components, where n is an integer. Thus we write the surface deformation $h(\mathbf{r},t)$ of our saturated waves as

$$h(\mathbf{r},t)=\frac{1}{4}\sum_{i=1}^{N}\sum_{n=-\infty}^{+\infty}A_{i,n}e^{\mathrm{i}[\mathbf{k}_i\cdot\mathbf{r}+(n+1/2)\Omega t]}+\text{c.c.}=\frac{1}{4}\sum_{i=1}^{N}(A_i e^{\mathrm{i}\mathbf{k}_i\cdot\mathbf{r}}+\text{c.c.})\sum_{n=-\infty}^{+\infty}[(\zeta_n+\varepsilon F_n)e^{\mathrm{i}(n+1/2)\Omega t}+\text{c.c.}]. \quad (2)$$

Here $\mathbf{r}=(x,y)$ is the horizontal coordinate. The set of *complex* Fourier coefficients ζ_n are the components of the eigenvector related to the linear stability problem and determine the subharmonic temporal behavior. F_n are unknown contributions from nonlinear interactions that can be determined by comparing our data with linear theory. The spatial modes are characterized by the wave-vectors $\mathbf{k}_i$, each carrying an individual *complex* amplitude A_i that are determined by the nonlinearities of the problem. In principle the wave-vector $\mathbf{k}_i$ can have any length and orientation but at onset the relation $|\mathbf{k}_i|=k_c$ holds. The number N of participating modes determines the degree of rotational symmetry of the pattern: $N=1$ corresponds to lines, $N=2$ to squares, $N=3$ to hexagons or triangles, etc. It can be shown [27] that the ζ_n and ζ_{-n} are coupled in a way such that $\zeta_{n-1}^*=\zeta_{-n}$ (* denotes the complex conjugate) so that heterodyning of right and left traveling waves always results in *standing* waves. Neglecting εF_n at small supercriticality ε Eq. (2) then reads

$$h(\mathbf{r},t)=\sum_{i=1}^{N}(|A_i|\cos[\mathbf{k}_i\cdot\mathbf{r}+\phi_i])\times\sum_{n=0}^{+\infty}|\zeta_n|\cos[(n+1/2)\Omega t+\psi_n], \quad (3)$$

where ϕ_i and ψ_n represent a set of the spatial and temporal phases. The complex eigenvectors ζ_n can be calculated and the ratio of the amplitudes $|\zeta_{n+l}|/|\zeta_n|$ as well as the temporal phases ψ_n can be compared with experimental data. They are obtained in the following way: For each step in the driving amplitude a series of snapshots of the surface state (Fig. 2) is taken. The primary pattern consists of squares and as mentioned above their formation is governed by the nonlinearities of the problem for which we cannot make any prediction.

The Fourier transformation, when applied to a temporal sequence of pictures, yields the temporal behavior of spatial amplitudes $A_i=A(\mathbf{k}(ij))$ that are shown in Figs. 4(a)–4(c). For the wave-vectors $\mathbf{k}(ij)$ crystallography notations are used, e.g., $\mathbf{k}(10)$ and $\mathbf{k}(01)$ are the vectors that generate the

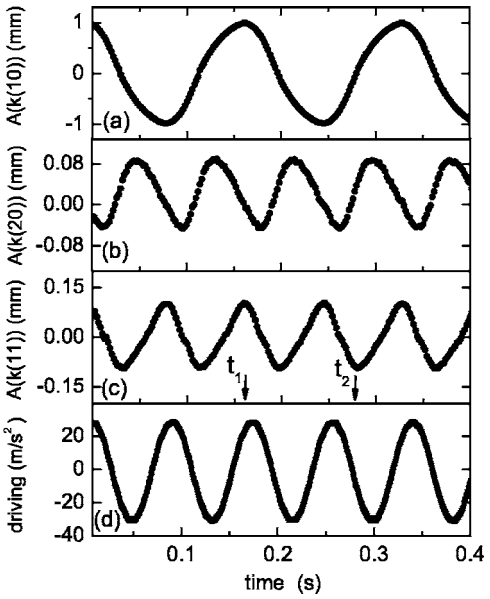

FIG. 4. Temporal behavior of amplitudes A corresponding to spatial modes $k(10)$ [(a)], $k(20)$ [(b)], and $k(11)$ [(c)] of the square Faraday pattern at $\Omega/2\pi=12$ Hz and $\varepsilon=0.17$ ($a_0=30.0$ m/s^2). (d) shows the driving signal $a(t)$. Please note, that in contrast to Ref. [2], not the square root of the power spectra but the amplitude A of the surface elevation $h(\mathbf{r},t)=A\cos[\mathbf{k}(ij)\cdot\mathbf{r}]$ is shown.

unit cell of the square pattern (Fig. 2). The temporal evolution of the amplitude of one of the critical modes $A[\mathbf{k}(10)]$ with $|\mathbf{k}(10)|=k_c$ [Fig. 4(a)] is then again Fourier transformed which results in a typical spectrum shown in Fig. 5(a). These data are taken for all driving strengths ε [Figs. 6(a) and 6(b)] and we always find the same values for the amplitudes of the symmetry equivalent modes $A(\mathbf{k}(10))$ and $A(\mathbf{k}(01))$ (not shown) within the experimental resolution. In agreement with former investigations [16] in a system with a larger aspect ratio (container size to wavelength) our study reveals that the fundamental spatial mode $|\mathbf{k}(10)|=k_c$ for all ε. We

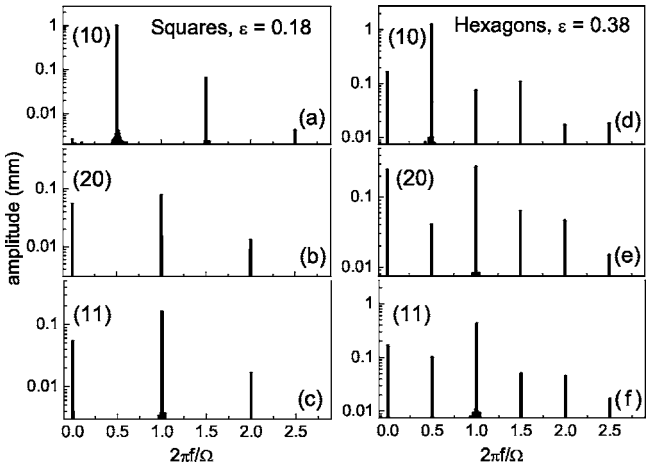

FIG. 5. Temporal Fourier spectra ($\Omega/2\pi=12$ Hz) of the amplitudes $A[\mathbf{k}(ij,\omega)]$ corresponding to several spatial modes of the oscillating square Faraday pattern [(a), (b), and (c)] ($\varepsilon=0.18$) and hexagonal Faraday pattern [(d), (e), and (f)] ($\varepsilon=0.38$).

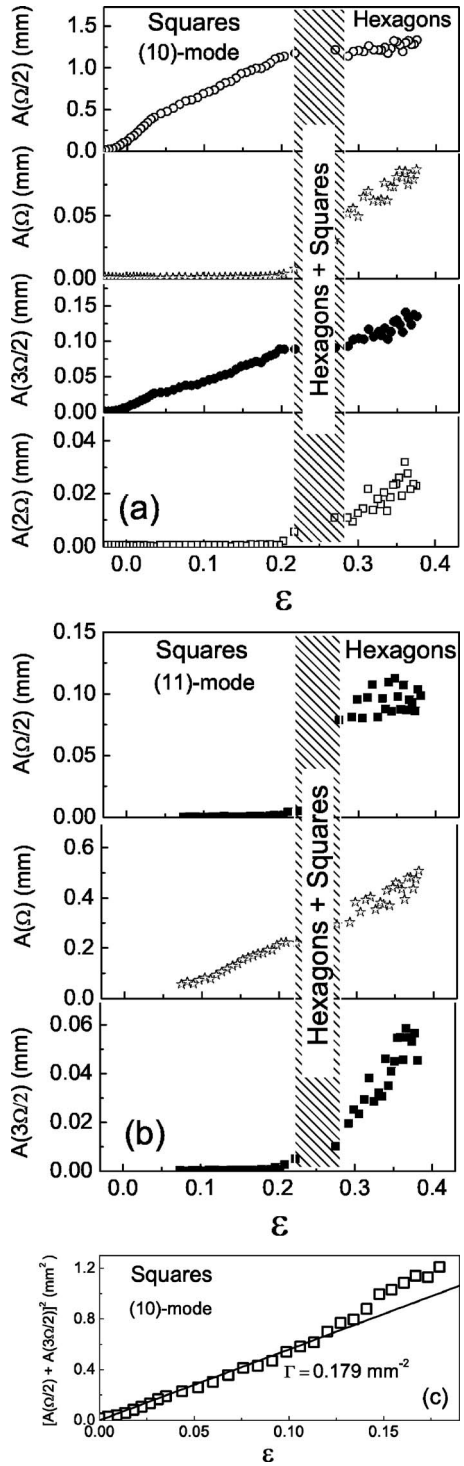

FIG. 6. Amplitudes $A(n\Omega/2)$ of the $\mathbf{k}(10)$ [(a)] and $\mathbf{k}(11)$ [(b)] modes at $\Omega/2\pi=12$ Hz as a function of the driving strength ε. (c) The square of the sum of the subharmonic components of the (10)-mode versus ε. As would be expected for a forward bifurcation the data can be linearly fitted, at least up to driving strength of $\varepsilon\approx0.1$

can now extract the ratio of $A(3\Omega/2,\mathbf{k}(10))/A(\Omega/2,\mathbf{k}(10))$ that is shown in the inset of Fig. 7 exemplarily for a frequency of $\Omega/2\pi=12$ Hz. Similarly, the theoretical values have been determined for the strongest growing mode that is

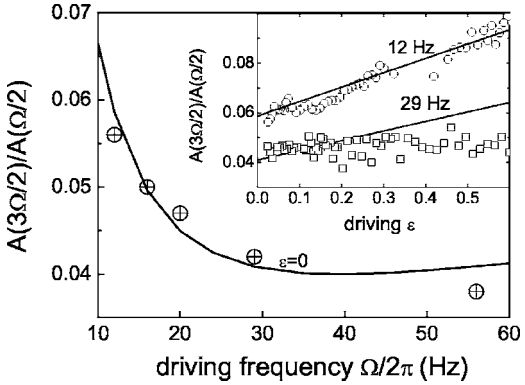

FIG. 7. Ratio of the amplitudes $A(3\Omega/2)/A(\Omega/2)$ of the $\mathbf{k}(10)$ mode at $\varepsilon=0$ for different driving frequencies. The symbols mark experimental, the lines data from the linear theory. The experimental data are extrapolated from measurements at $\varepsilon>0$ shown in the inset: The amplitude ratios at $\Omega/2\pi=12$ and 29 Hz as a function of the driving strength ε.

found to be equal to the critical mode within reasonable resolution. The contribution of the $(3\Omega/2)$ component is of the order of 5 to 10% and increases slightly with the driving strength. The agreement between the experiment and linear theory is astonishingly good up to driving strength $\varepsilon>0.5$, especially for lower driving frequencies. This means that the contributions F_n are weak and surprisingly the good agreement even holds up to secondary patterned surface states, where a transition from a square to a hexagonal state takes place and, as will be shown later, rather strong nonlinear contributions participate in the overall dynamics of the system. The experimental data show also that at driving strength as low as $\varepsilon=0.02$ the surface state oscillates with frequencies $(n+1/2)\Omega$ but contains no measurable higher spatial Fourier modes [see Fig. 6(b)] in perfect agreement with the linear theory. This allows an extrapolation of $A(3\Omega/2,\mathbf{k}(10))/A(\Omega/2,\mathbf{k}(10))$ to the critical region $(\varepsilon=0)$ for all driving frequencies Ω (Fig. 7). The amplitude ratio decreases first with increasing frequency and then passes a minimum at $\Omega/2\pi\approx40$ Hz. This characteristic shape reflects the amount of damping which is present in the system. At low driving frequencies the ratio between fill height and the wave number is small. In this regime the damping from the bottom of the container, which increases as the frequency is lowered, is the most significant contribution. For higher driving frequencies the damping from the bulk of the liquid (an increasing function with the frequency) becomes dominant. This behavior is also reflected in the critical accelerations [see Fig. 3(a)]. The ratio $A(5\Omega/2,\mathbf{k}(10))/A(\Omega/2,\mathbf{k}(10))$ has been evaluated too, but the experimental resolution is not sufficient any more for a conclusive comparison between theory and experiment.

In the same way the temporal phases ψ_n can be extracted from the Fourier spectrum (Fig. 8) and also here a good agreement between the theoretical predictions and experimental data is obtained, at least for the fundamental $\Omega/2$ component. For the $3\Omega/2$ component the scatter of the experimental data is very large and we find significant differences between experiment and theory, probably due to nonlinear interactions.

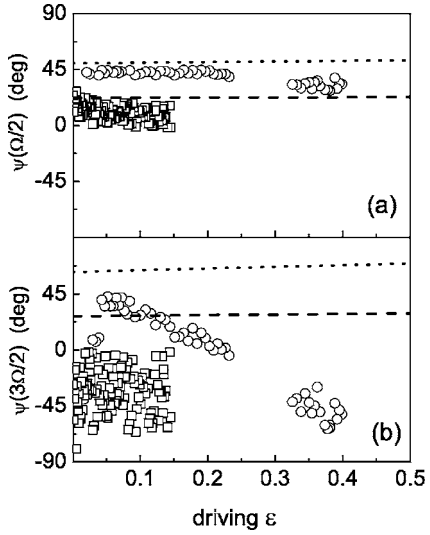

FIG. 8. Temporal phases $\psi(\Omega/2)$ [(a)] and $\psi(3\Omega/2)$ [(b)] of the $\mathbf{k}(10)$ mode for two driving frequencies versus driving strength ε. The symbols are the experimental data, the lines are the theoretical calculations. Squares and broken line: $\Omega/2\pi=57$ Hz; circles and dotted line: $\Omega/2\pi=12$ Hz. In the range $0.2<\varepsilon<0.28$ a transition from squares to hexagons takes place leading thus to a disordered state. For this reason an extraction of the phases is not possible there.

IV. NONLINEAR SURFACE STATE AT $\Omega=12$ Hz

A. Square state

The primary pattern near onset $(0<\varepsilon<0.28)$ consists of squares, shown in Fig. 2. Its formation is determined by the minimum of the Lyaponov functional. The corresponding amplitude equation of the critical modes [26] and a quantitative theoretical prediction of the expected pattern can be given by inspection of the cubic coupling coefficient [4,5]. To our knowledge, for a two liquid system there have not yet been attempts to calculate this coefficient. The amplitude equations follow from a solvability condition of the weakly nonlinear analysis of the underlying constitutive equation and its principle form is already determined by the symmetry of the system. For the subharmonic response one can write

$$\tau\partial_t A(\mathbf{k}_i)=\epsilon A(\mathbf{k}_i)-\sum_{j=1}^{N}\Gamma(\theta_{ij})|A(\mathbf{k}_j)|^2A(\mathbf{k}_i), \qquad (4)$$

where τ is the linear relaxation time and $\Gamma(\theta_{ij})$ is the cubic coupling coefficient which depends on the angle θ_{ij} between the modes $\mathbf{k}_i$ and $\mathbf{k}_j$. The temporal spectra of spatial amplitudes $A(\mathbf{k}_i)$ are characterized only by subharmonic components $(n+1/2)\Omega$ given by the ζ_n from the linear eigenvectors. Equation (4) predicts a pitchfork bifurcation and in order to study this scenario one has to first extract the different temporal Fourier modes of the measured time dependence of $A(\mathbf{k}_i)$ (Fig. 4). The result is shown in Figs. 5(a) and 6(a). As long as the pattern consists of squares there is no harmonic response in the basic spatial modes to observe, but a continuous growth of $\Omega/2$ and $3\Omega/2$ components only. The $5\Omega/2$ component is very weak and only slightly larger

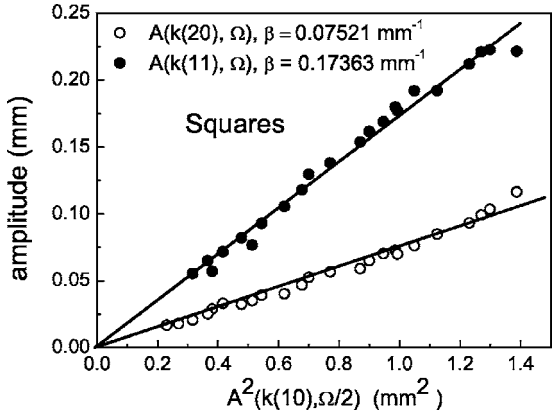

FIG. 9. Amplitudes $A[\mathbf{k}(20)]$ and $A[\mathbf{k}(11)]$ versus the square of the amplitude of the fundamental mode $A[\mathbf{k}(10)]$ ($\Omega/2\pi=12$ Hz). Coefficient β is the slope of the linear fit and characterizes the efficiency of the nonlinear interaction.

than the noise. The square of the sum of the amplitudes $A_s=A(\Omega/2)+A(3\Omega/2)$ yields a straight line if plotted versus the driving strength ε [Fig. 6(c)] as would indeed be expected for the case of a pitchfork bifurcation. Since $A_s^2=\varepsilon/\Gamma$ one can extract the cubic coupling coefficient from the slope, and we find $\Gamma=0.179$ mm^{-2}.

Now we can inspect the next higher harmonic spatial modes $A(\mathbf{k}(11))$ and $A(\mathbf{k}(20))$. Their temporal behavior is shown in Figs. 4(b) and 4(c), respectively. Both modes are a result of an interaction of three modes related to the wave vectors which satisfies the spatial resonant condition, e.g., $\mathbf{k}(11)+\mathbf{k}(\bar{1}0)+\mathbf{k}(0\bar{1})=0$ and $\mathbf{k}(20)+\mathbf{k}(\bar{1}0)+\mathbf{k}(\bar{1}0)=0$. As a natural consequence of such nonlinear spatial wave interaction they obey harmonic oscillations, shown in Figs. 5(b) and 5(c). The striking result of our analysis is rather the constant offset that we find in the $A(\mathbf{k}(11))$ and $A(\mathbf{k}(20))$ spectrum [see Figs. 4(b) and 4(c)] resulting in zero frequency contributions in the temporal spectra presented in the Figs. 5(b) and 5(c). This means that in addition to the oscillatory part the interfacial profile contains always contributions of static deformations of the form $h(\mathbf{r},t)=|A_i|\cos(\mathbf{k}_i\cdot\mathbf{r})$, with $\mathbf{k}_i=\mathbf{k}(11),\mathbf{k}(20)$. This might be a surprising result, even if the mass conservation is not violated. In fact, this is just a simple consequence of the quadratic coupling of a *real* standing surface wave oscillation [5], i.e. $[A_1\cos(\Omega t/2)\cos(\mathbf{k_i}\cdot\mathbf{r})]^2$ gives in particular contribution $\propto A_1^2(1+\cos\Omega t)\cos(2\mathbf{k}_i\cdot\mathbf{r})$ [compare also with Fig. 14(c)].

This quadratic coupling scheme can be verified by plotting $A(\mathbf{k}(20))$ and $A(\mathbf{k}(11))$ versus the square of the amplitude of the fundamental mode $A(\mathbf{k}(10))$ (or versus the product of symmetry equivalent modes, i.e. $A(\mathbf{k}(10))\times A(\mathbf{k}(01))=A(\mathbf{k}(10))^2$ within the experimental resolution). The data can be perfectly reproduced by a linear fit (see Fig. 9). From the slope one gets the efficiency β of this nonlinear coupling which we find to be nearly the same in value for all frequencies ($\Omega/2\pi=12$, 16, 20, and 29 Hz) where square patterns were observed. Finally our Fourier analysis yields that the imaginary part of the coupling scheme obeys the same resonance conditions, and the spatial phases of the higher harmonic modes are given by $\phi(\mathbf{k}(20))=2\phi(\mathbf{k}(10))$ and $\phi(\mathbf{k}(11))=\phi(\mathbf{k}(10))+\phi(\mathbf{k}(01))$.

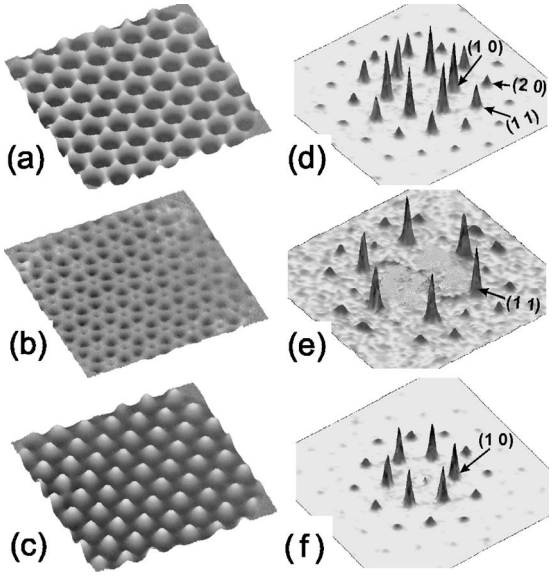

FIG. 10. Snapshots of the hexagonal Faraday pattern [(a), (b), and (c)] and corresponding power spectra [(d), (e), and (f), respectively] at $\Omega/2\pi=12$ Hz and $\varepsilon=0.37$ ($a_0=39.3$ m/s^2) for three different temporal phases. (a) Down hexagons; (b) pattern near the minimal surface elevation, (c) up hexagons. See Refs. [2,13] for further explanations on the switch from up to down hexagons in the Faraday Experiment.

B. Hexagonal state

In the range ($0.20<\varepsilon<0.28$) the pattern becomes disordered and at higher driving accelerations transforms to a hexagonal state (see Fig. 10) that consists of three fundamental spatial Fourier modes $\mathbf{k}_{1,2,3}$. It should be mentioned that for the construction of the crystallographic unit cell two basis vectors $\mathbf{k}(10)$ and $\mathbf{k}(01)$ are sufficient thus $\mathbf{k}_1=\mathbf{k}(10)$, $\mathbf{k}_2=\mathbf{k}(\bar{1}1)$, and $\mathbf{k}_3=\mathbf{k}(\bar{1}1)+\mathbf{k}(10)=\mathbf{k}(0\bar{1})$, as indicated in Fig. 11.

The surface elevation profile in the hexagonal state also reveals the striking offset of static sinusoidal surface deformation, but in contrast to square patterns, both harmonic and subharmonic responses contributions are presented in tempo-

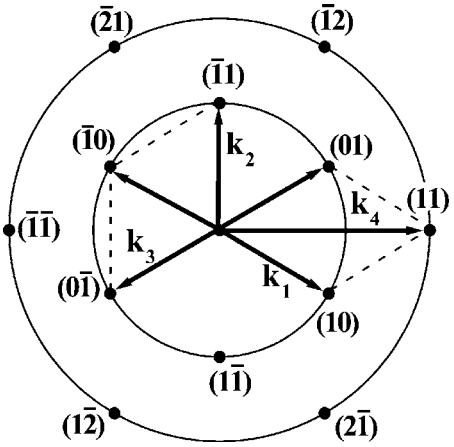

FIG. 11. Vector diagram of the interacting modes for the hexagonal surface state.

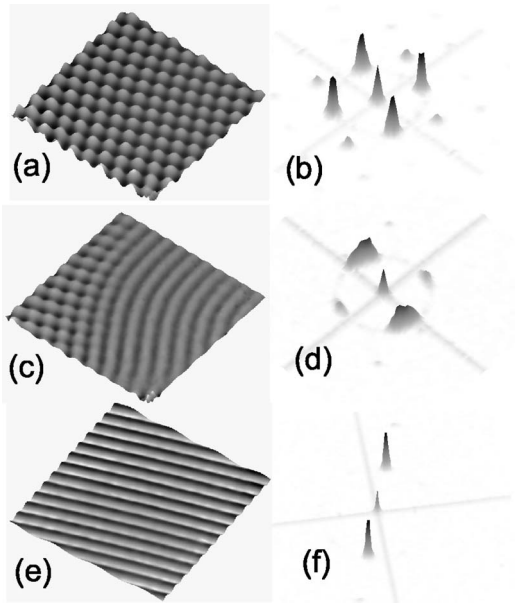

FIG. 12. Snapshots of the Faraday pattern [(a),(c), and (e)] and the power spectra [(b), (d), and (f)] at $\Omega/2\pi=20$ Hz and $\varepsilon=0.6$ ($a_0=54.4$ m/s^2) [(a),(b)]; $\Omega/2\pi=20$ Hz and $\varepsilon=0.08$ ($a_0=36.7$ m/s^2) [(c),(d)]; $\Omega/2\pi=57$ Hz and $\varepsilon=0.11$ ($a_0=116.3$ m/s^2) [(e),(f)].

ral Fourier spectra [see Figs. 5(d)–5(f) and Figs. 6(a) and 6(b)]. While the harmonic ($n\Omega$) temporal component in the higher spatial harmonics $\mathbf{k}(20)$ and $\mathbf{k}(11)$ appear in a similar manner as for the square pattern, the spatial resonance condition $\mathbf{k}(10)+\mathbf{k}(0\bar{1})=\mathbf{k}(1\bar{1})$ results in harmonic ($n\Omega$) contributions in the critical mode $|\mathbf{k}(1\bar{1})|=k_c$. Consequently harmonic ($n\Omega$) and subharmonic $[(n+1/2)\Omega]$ components of the fundamental modes together couple back thus leading to the appearance of subharmonic response in the higher spatial modes $\mathbf{k}(20)$ and $\mathbf{k}(11)$. It must be stressed that the harmonic contributions do not appear in the temporal spectra of the linear unstable modes k_c and quadratic interactions of ($n\Omega/2$) components do not appear in the amplitude equations. Nevertheless the hexagonal state allows for a *spatial* resonance between linear unstable modes. In other words, this means that we have here the interesting case where the system has a broken temporal symmetry within the framework of the weakly nonlinear approximation that is driven by spatial resonance only. This symmetry break is not observed in the quadratic state, where spatial resonance between linear unstable modes is forbidden. This particular violation of the weakly nonlinear resonance conditions can best be seen in Fig. 6(a) where the components of harmonic response of the fundamental spatial mode with $|\mathbf{k}(\mathbf{10})|=k_c$ clearly occurs after the transition from squares to hexagons is realized. A similar behavior for subharmonic components of the higher spatial modes is observed [see e.g., Fig. 6(b) for $|\mathbf{k}(\mathbf{11})|=\sqrt{3}k_c$].

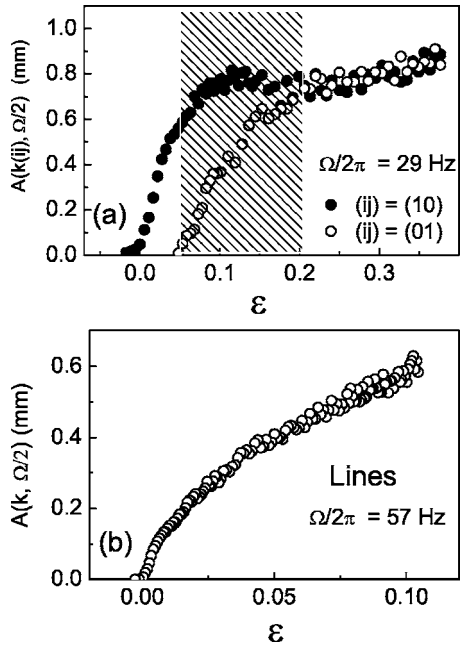

FIG. 13. Amplitudes $A(\Omega/2)$ of the $\mathbf{k}(10)$ and $\mathbf{k}(01)$ modes at $\Omega/2\pi=29$ Hz [(a)], and $\mathbf{k}(1)$ mode at $\Omega/2\pi=57$ Hz [(b)] as a function of the driving strength ε. The marked strip in (a) indicates the region of the crossed rolls state.

V. PATTERN DYNAMICS AT $\Omega/2\pi>12$ Hz

The pattern dynamics at driving frequencies $\Omega/2\pi>12$ Hz is characterized by a transition to a line pattern. At $\Omega/2\pi=16$ Hz the pattern still consists of squares only whereas at $\Omega/2\pi=20$ and 29 Hz the primary pattern consists

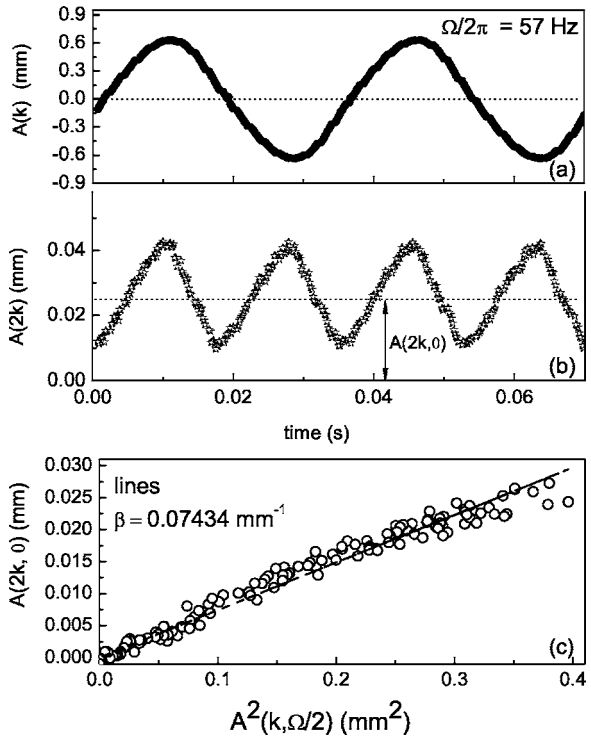

FIG. 14. The amplitudes of spatial modes $A(k)$ [(a)] and $A(2k)$ [(b)] in the line state at $\Omega/2\pi=57$ Hz and $\varepsilon=0.11$ ($a_0=116.3$ m/s^2). The temporal constant offset in (b) is indicated by $A(2k,0)$. (c) shows the dependence of $A(2k,0)$ versus $A^2(k,\Omega/2)$.

of lines, which are sometimes slightly distorted [Figs. 12(c) and 12(d)]. But at higher driving strength ε a second Fourier mode, perpendicular to the first one, starts to grow [Fig. 13(a)] and we observe a "crossed roll" state which transforms at highest ε into a pure square state. For $\Omega/2\pi = 57$ Hz a pure line state is stable for all driving strengths [see Figs. 12(e), 12(f), and 13(b)]. A pronounced static offset in the temporal behavior of $A(2\mathbf{k})$ mode [Fig. 14(b)] is here even larger than the temporal oscillation amplitude and $A(2\mathbf{k},t)$ thus never crosses the zero line. Similarly, as was shown for the $A(\mathbf{k}(20),\Omega)$ or $A(\mathbf{k}(11),\Omega)$ modes in the square state, this quadratic coupling scheme holds also for the zero frequency (static) component as shown in Fig. 14(c).

VI. CONCLUSION

We have demonstrated a technique to quantitatively measure the spatiotemporal Fourier spectrum of Faraday waves on a two liquid interface. With this technique it is possible to test theoretical predictions, especially from numerical simulations. To our knowledge there has still been no full Navier Stokes numerical simulation made of the 3D problem and quantitative tests for future work are most important and thus we would like to encourage such attempts. But with our technique we are also able to verify known predictions from the linear stability analysis and we find good agreement up to high driving strength of $\varepsilon \approx 0.5$. In the nonlinear state the most pronounced result is the identification of significant temporal static spatial surface deformations. With our possibility to access any Fourier component separately we can identify several resonance mechanisms, including an interesting case of a temporal resonance violation in the framework of the weakly nonlinear theory by use of spatial resonances.

ACKNOWLEDGMENT

This work was supported by the German Science Foundation Project No. Mu 912.

[1] M. Faraday, Philos. Trans. R. Soc. London **52**, 319 (1831).
[2] A. Kityk, H. W. Müller, K. Knorr, and C. Wagner, Europhys. Lett. **65**, 857 (2004).
[3] K. Kumar and L. S. Tuckerman, J. Fluid Mech. **279**, 49 (1994).
[4] W. Zhang and J. Viñals, J. Fluid Mech. **336**, 301 (1997).
[5] P. Chen and J. Viñals, Phys. Rev. E **60**, 559 (1999).
[6] For a review see: J. W. Miles and D. Henderson, Annu. Rev. Fluid Mech. **22**, 143 (1990); H. W. Müller, R. Friedrich, and D. Papathanassiou, in *Theoretical and Experimental Studies of the Faraday Instability*, Lecture Notes in Physics, edited by F. Busse and S. C. Müller (Springer, Berlin, 1998).
[7] S. T. Milner, J. Fluid Mech. **225**, 81 (1990).
[8] B. Christiansen, P. Alstrom, and M. T. Levinsen, Phys. Rev. Lett. **68**, 2157 (1992).
[9] W. S. Edwards and S. Fauve, J. Fluid Mech. **278**, 123 (1994).
[10] D. Binks and W. van de Water, Phys. Rev. Lett. **78**, 4043 (1997).
[11] A. Kudrolli and J. P. Gollub, Physica D **97**, 133 (1997).
[12] C. Wagner, H. W. Müller, and K. Knorr, Phys. Rev. Lett. **83**, 308 (1999).
[13] C. Wagner, H. W. Müller, and K. Knorr, Phys. Rev. E **62**, R33 (2000).
[14] A. Kudrolli, B. Pier, and J. P. Gollub, Physica D **123**, 99 (1998).
[15] H. Arbell and J. Fineberg, Phys. Rev. Lett. **81**, 4384 (1998).
[16] A. Wernet, C. Wagner, D. Papathanassiou, H. W. Müller, and K. Knorr, Phys. Rev. E **63**, 036305 (2001).
[17] W. B. Wright, R. Budakian, and S. J. Putterman, Phys. Rev. Lett. **76**, 4528 (1996).
[18] R. Richter and J. Bläsing, Rev. Sci. Instrum. **72**, 1729 (2001).
[19] M.-T. Westra, D. J. Binks, and W. van de Water, J. Fluid Mech. **496**, 1 (2003).
[20] M. Lommer and M. T. Levinsen, J. Fluoresc. **12**, 45 (2001).
[21] H. Arbell and J. Fineberg, Phys. Rev. E **65**, 036224 (2002).
[22] C. R. Tipton and T. Mullin, Phys. Fluids **16**, 2336 (2004).
[23] D. Binks, M.-T. Westra, and W. van de Water, Phys. Rev. Lett. **79**, 5010 (1997).
[24] J. Bechhoefer, V. Ego, S. Manneville, and B. Johnson, J. Fluid Mech. **288**, 325 (1995).
[25] H. W. Müller, H. Wittmer, C. Wagner, J. Albers, and K. Knorr, Phys. Rev. Lett. **78**, 2357 (1997).
[26] M. C. Cross and P. C. Hohenberg, Rev. Mod. Phys. **65**, 851 (1993).
[27] S. Douady and S. Fauve, Europhys. Lett. **10**, 309 (1989).